Modelling porous coastal structures using a level set method based VRANS-solver on staggered grids

Athul Sasikumar[1], Arun Kamath, *[2], and Hans Bihs[2]

[2]Department of Civil and Environmental Engineering, Norwegian University of Science and Technology (NTNU), 7491 Trondheim, Norway
[1]Norconsult AS, Trondheim, Norway

Coastal Engineering Journal, 2020, , pp. -.
DOI: http://dx.doi.org/10.1080/21664250.2020.1734412

Abstract

Several engineering problems in the field of coastal and offshore engineering involve flow interaction with porous structures such as breakwaters, sediment screens and scour protection devices. In this paper, the interaction of waves with porous coastal structures using an open-source computational fluid dynamics (CFD) model is presented. The fluid flow though porous media is modelled using the Volume-averaged Reynolds-averaged Navier-Stokes (VRANS) equations. Novel improvements to the numerical grid architecture and discretisation schemes are made, with a staggered numerical grid for better pressure-velocity coupling and higher-order schemes for convection and time discretisation. New interpolation schemes required for the VRANS equations on a staggered grid are implemented. The flow problem is solved as a two-phase problem and the free surface is captured with the level set function. The model is validated by comparing the numerical results to experimental data for different cases such as flow though crushed rock, solitary and regular wave interaction with a porous abutment and wave interaction with a breakwater considering the three different porous layers. The numerical results are also seen to be highly grid independent according to the grid convergence study and show a significantly better agreement to experimental data in comparison to current literature.

Keywords: VRANS ; Numerical wave tank; Porous; Breakwater; CFD; REEF3D

*Corresponding author,arun.kamath@ntnu.no
Postprint, published in Coastal Engineering Journal, doi:http://dx.doi.org/10.1080/21664250.2020.1734412

1 Introduction

One of the important hydrodynamic processes in the coastal regions is the interaction of water waves with permeable coastal structures such as breakwaters. A rubble mound breakwater typically consists of a core layer, which is covered by filter layers to protect core material from erosion and then the outermost armour layer. Wave interaction with such structures has generally been investigated using model tests and empirical coefficients have then been determined to describe the flow. Recent advances in computing power have presented a great opportunity to obtain further insight into the hydrodynamic processes in the coastal zone using advanced numerical modelling approaches. There are several approaches to numerical modelling of the hydrodynamics of coastal structures, such as nonlinear shallow water equations (Kobayashi and Wurjanto, 1989; Hu et al., 2000) Boussinesq-type equations (Madsen et al., 1991; Fuhrman et al., 2005; Engsig-Karup et al., 2008; Liu et al., 2018), smoothed particle hydrodynamics (Shao, 2010; Gui et al., 2015; Ren et al., 2016) and Reynolds averaged Navier-Stokes (RANS) equations (Li et al., 2004; Higuera et al., 2013; Kamath et al., 2017*a*) to name a few. A large amount of progress has been achieved in the last decade in the numerical modelling of wave-structure interaction based on the RANS equations. This suggests that these models will become increasingly important for coastal engineers, as few simplifying assumptions are made compared to other approaches. In literature, the flow through porous media is classified based on the Reynolds number calculated based on pore size and pore velocity into Darcy flow, Forchheimer flow, unsteady laminar and fully turbulent flow (Dybbs and Edwards, 1984). For these different classes, different formulations are proposed for the calculation of the flow (Darcy, 1856; Forchheimer, 1901; Polubarinova-Kochina, 1962). They have a relatively narrow range of applicability within the flow regimes that are assumed in the derivation of the relations and highly dependent on the associated empirical coefficients. The challenge lies in quantifying the flow through porous media while not resolving the flow through every single pore in the volume.

As an advance in modelling of coastal structures based on the RANS equations, a method for analysing flow through porous breakwater layers was proposed by van Gent (1995), where the effects of the porous medium is included through resistance coefficients. Liu et al. (1999) implemented the same method in their work. The resistance coefficients formulated in these works are still relevant and are relied on for the modelling of porous media in current literature. In order to account for the intrinsic flow through the randomly arranged pores, volume averaged RANS (VRANS) equations were introduced (Hsu et al., 2002). This formulation was later applied in two-dimensional models to evaluate wave interaction with low crested and submerged porous structures (Garcia et al., 2004; Lara et al., 2006).

Furthermore, del Jesus et al. (2012) presented a three-dimensional VRANS model with a new implementation of the governing equations to provide a general approach to modelling porous media with more appropriate assumptions. The resistance terms are based on the relations between Darcy-Forchheimer coefficients and physical parameters such as grain diameter and porosity (Engelund, 1953). Turbulence modelling for the flow through porous media is accounted for through a volume averaged $k-\omega$ SST model. A similar approach was included in OpenFOAM by Higuera et al. (2014). Further changes to the continuity and momentum equations were introduced by Jensen et al. (2014) for a more physically correct implementation, similar to that shown by Hsu et al. (2002). The eddy-viscosity in the porous media is not considered as wave breaking near the structure was not expected. The validation of the

VRANS model for irregular wave interaction with a breakwater was presented by Jacobsen et al. (2015). The aforementioned developments in the area of porous media modelling using RANS equations shows the relevance of the field and the scope for further research.

The modelling approaches in current literature are mostly based on a collocated unstructured grid architecture in a finite volume framework with second-order schemes for spatial and temporal discretisation and a volume of fluids method to obtain the free surface. An novel numerical approach to the grid architecture and discretisation schemes can improve the modelling accuracy of porous coastal structures. A structured grid allows for easy implementation of higher-order schemes which provide more accurate results. In addition, accurate calculation of the pore pressures is essential to obtain a good representation of the fluid-porous media interaction. This can be achieved through the use of a staggered grid that allows for better pressure-velocity coupling. Along with the use of an immersed boundary method, complex geometries can be modelled on a staggered structured grid. The level set method provides a sharp interface which helps in the sharp representation of the fluid-porous media interface. Additional interpolation schemes to account for the porous media relations between the different interfaces between the fluid and porous media and porous media of different characteristics are then required. With the aforementioned implementation, a consistent, numerically stable and accurate model for porous media interaction can be built.

In the current study, wave interaction with porous media is simulated using the open-source hydrodynamics model REEF3D (Bihs et al., 2016). The model is based on a finite difference framework with a staggered structured numerical grid and obtains the free surface using the level set method. The model has been previously applied to study several complex free surface phenomena such as focussed wave forces (Bihs et al., 2017), hydrodynamics of semi-submerged cylinders (Ong et al., 2017), water impact and entry (Kamath et al., 2017*b*) and floating bodies in waves (Bihs and Kamath, 2017). The wave interaction with a impervious submerged step is simulated and the wave kinematics are compared to data obtained from experiments carried out at NTNU Trondheim. In order to validate the VRANS implementation in the model, a 2D dam break case through porous media from the experiments carried out by Liu et al. (1999) is replicated in this study. Wave interaction with a porous abutment is simulated using both solitary and regular waves. The numerical results for the free surface and pore pressure are compared to the experimental data from Lara et al. (2012). Regular wave interaction with a rubble mound breakwater with core, filter and armour layers is simulated and the calculated pore pressures in the different layers are compared to the measured values from the experiments conducted at the hydraulic laboratory at SINTEF/NTNU in Trondheim (Arntsen et al., 2003). The study presents a novel numerical approach to modelling flow though porous media while building upon previous works by Jensen et al. (2014) for the VRANS formulation. The current paper extends the current state-of-the-art to numerical implementation on a staggered grid with the ghost cell immersed boundary method and the level set method for the free surface to provide an improved representation of both the free surface features and the pore pressures under wave interaction with porous coastal structures. The robustness of the model is demonstrated through free surface and pore pressure calculations in various case scenarios with porous objects of different shapes and with multiple porous layers.

2 Numerical Approach

2.1 VRANS equations

When modelling flow through porous media, the presence of grains and voids and their effect on the flow is described as a resistance to the flow that dissipates energy. Darcy (1856) stated that the flow velocity in the porous medium is proportional to the pressure gradient I as shown in Eq. 1.

$$I = au^f \tag{1}$$

where, a is the inverse of hydraulic conductivity K which represents the permeability of the porous medium and u^f is the filter velocity in the $x-$ direction. The filter velocity is the actual pore velocity averaged over the pores and is defined in Eq. 2.

$$u_f = \frac{1}{A}\int\int udA = n.u \tag{2}$$

where A is the cross sectional area of the porous medium, u is the actual pore velocity, n is the porosity, which can be expressed as the ratio of the pore volume to the total volume, $n = V_{pore}/V_{total}$.

This formulation is only applicable for laminar flow where pore sizes and velocities are small and the linear relationship is not valid when these quantities increase. In the case of flow through coarse material, Forchheimer (1901) included friction terms and the pressure gradient is composed of a linear term that relates to the laminar flow. Turbulent flow is included by the non-linear term as shown in Eq. 3.

$$I = au^f + bu^f \left|u^f\right| \tag{3}$$

where a and b are dimensionless coefficients referred to as friction factors. These factors depend on the fluid viscosity, the specific granular composition of the porous medium and the flow regime. This means that the factors a and b are not constants for a given material and are influenced by the Reynolds number (Re). The Forchheimer relations are empirical, but can also be derived from the Navier-Stokes equations (Burcharth and Christensen, 1995). These relations are valid only in the case of stationary flow and an inertia term for unsteady flow was suggested by Polubarinova-Kochina (1962), given in Eq. 4.

$$I = au^f + bu^f \left|u^f\right| + c\frac{\partial u^f}{\partial t} \tag{4}$$

where c is also a coefficient applied in case of local accelerations. Dybbs and Edwards (1984) identified four main flow regimes based on the Reynolds number $Re = u^p D_p/v$ related to the pore size D_p and pore velocity u^p shown in Table (1). By incorporating the porous media equations into the RANS equations, different flow regimes can be evaluated without the limitations of the individual equations discussed above.

Table 1: Porous flow regimes

Regime	Re - range	Flow characteristics
Darcy flow	Re<1-10	Flow dominated by viscous forces, velocity distribution depends on local geometry
Forchheimer flow	1-10<Re< 150	Development of an inertial 'core' flow outside the boundary layers
Unsteady laminar flow	150<Re<300	Transitional flow regime between inertial, Forchheimer and fully turbulent flow
Fully-turbulent flow	300<Re	Highly unsteady and chaotic flow regime

An illustration of the volume averaging process is provided in Fig. (1). The surface S includes both the solid phase and the fluid phase, and creates the averaging volume with the radius r. The total volume V remains the same while the actual volume of the fluid phase may vary depending on the position of averaging volume. The volume averaging process is applied with the length scale constraints defined by $l \ll r \ll L$, where l is the pore length scale and L is the macroscopic length scale.

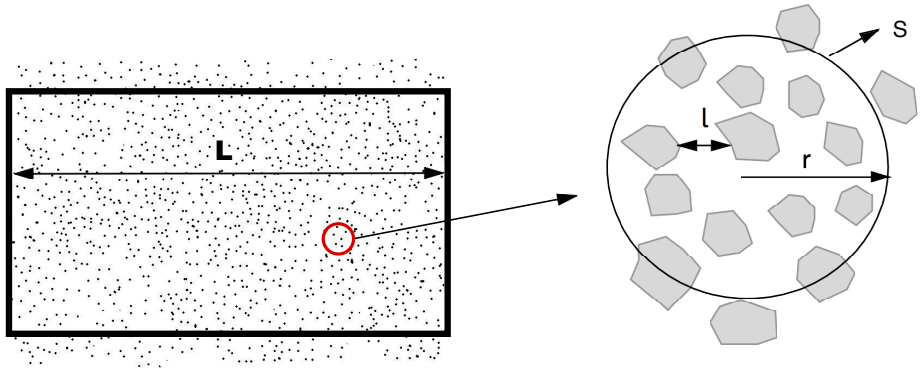

Figure 1: Volume averaging in porous media

From current literature, it is evident that there is no unique method for volume averaging the RANS equations to model porous media flow. In this study, Volume-averaged Reynolds-Averaged Navier-Stokes equations (VRANS) formulation proposed by Jensen et al. (2014) is chosen and implemented in a finite difference framework for a staggered numerical grid using higher-order discretisation schemes. Additional interpolations required for the implementation on such a grid architecture. For the purpose of volume averaging, the velocity at a point is assumed to consist of an ensemble average velocity ($\overline{u_i}$) and a temporally fluctuating velocity ($u_i^{'}$) as shown in Eq. 5. When volume averaging is applied to an ensemble average value, it is convenient to introduce the velocity decomposition as shown in Eq. 6 (Gray, 1975).

$$u_i = \overline{u_i} + u_i^{'} \tag{5}$$

$$\overline{u_i} = \langle \overline{u_i} \rangle^f + u_i^{"} \tag{6}$$

where $\langle\overline{u_i}\rangle^f$ is the intrinsic volume averaged value and $u_i^{"}$ is the spatial fluctuation, $\langle\rangle$ denotes the volume averaged over the entire control volume including solids and $\langle\rangle^f$ denotes the volume averaged over pore volume only.

Applying the volume averaging theorem to the continuity equation together with the assumption that the velocities on the solids being zero results in Eq. 7. Here $\langle\bar{u}_i\rangle$ is the velocity averaged over the volume, called the filter velocity. The correct representation of the continuity equation for porous media is that the divergence of the filter velocity is zero, $\Delta\langle\bar{u}\rangle = 0$. This keeps the filter velocity constant in the flow direction and result in a zero flux for the velocity field when averaged over the entire volume, providing a divergence free velocity field.

$$\frac{\partial\langle\bar{u}_i\rangle}{\partial x_i} = 0 \tag{7}$$

Similarly, each term is volume averaged for the momentum equations. The formulations are based on filter velocities which are divided by the porosity to get the correct momentum contributions as shown in Eq. 8. The use of a filter velocity in the momentum equations results in different values for pressure gradients both inside and outside the porous media. So, the pressure is defined as the pore pressure in the momentum equations so that the hydrostatic pressure distribution both inside and outside are linear and identical.

$$(1+C_m)\frac{\partial}{\partial t}\frac{\langle\bar{u}_i\rangle}{n} + \frac{1}{n}\frac{\partial}{\partial x_j}\frac{\langle\bar{u}_i\rangle\langle\bar{u}_j\rangle}{n} = -\frac{1}{\rho}\frac{\partial\langle\bar{p}\rangle^f}{\partial x_j} + \frac{1}{n}\frac{\partial}{\partial x_j}\nu\left(\frac{\partial\langle\bar{u}_i\rangle}{\partial x_j} + \frac{\partial\langle\bar{u}_j\rangle}{\partial x_i}\right) + g_j + F_i \tag{8}$$

where C_m is the added mass coefficient which takes into account the grain-water interaction, calculated as shown in Eq. 9 (van Gent, 1993).

$$C_m = \gamma_p\frac{1-n}{n} \tag{9}$$

where n is the porosity and empirical coefficient γ_p =0.34, F_i represents the effect of turbulence in terms of additional resistance, which is modelled using the extended Darcy-Forchheimer equation including linear, non-linear forces and inertial forces for local accelerations as shown in Eq. 10.

$$F_i = -a\rho\langle\overline{u_i}\rangle - b\rho\sqrt{\langle\overline{u_j}\rangle\langle\overline{u_j}\rangle\langle\overline{u_i}\rangle} \tag{10}$$

where a and b are the resistance coefficients, theoretically described in Eqs. 11 and 12 following van Gent (1993).

$$a = \alpha\frac{(1-n)^2}{n^3}\frac{v}{\rho d_{50}^2} \tag{11}$$

$$b = \beta(1+\frac{7.5}{KC})\frac{(1-n)}{n^3}\frac{1}{d_{50}} \tag{12}$$

where d_{50} is the grain diameter and KC is the Keulegan-Carpenter number, which indicates the stationarity of the flow as a ratio between the turbulence and inertia effects. The coefficients α and β depend on the Reynolds number, shape of the stones, permeability and grade of porous material and have to be determined through experiments. A broad overview of the values of α and β is given by Troch (2000), comprising of publications by various authors using different types of materials in laminar, fully turbulent, steady and unsteady flow conditions.

The precise description of α and β coefficients are still not fully understood. Different values for these coefficients have been suggested based on experiments incorporating the effect of an oscillating flow via the KC number (van Gent, 1995; Burcharth and Christensen, 1995). It has been generally experienced over the years that under oscillatory flow and waves propagating over slopes or breaking, values existing in literature may not be valid anymore. In the absence of predictive methodology to determine the values of α and β, calibration has to be performed.

2.2 Numerical model

The VRANS equations described above are implemented in the open-source CFD model REEF3D (Bihs et al., 2016). The accurate modelling of wave-structure interaction requires higher order discretisation schemes and a sharp representation of the free surface. This is accomplished with the conservative fifth-order WENO scheme (Jiang and Shu, 1996) for discretising the convective terms in the momentum equations. The pressure is treated using Chorin's projection method (Chorin, 1968) and the resulting Poisson pressure equation is solved using a geometric multigrid preconditioned Bi-Conjugate Gradients Stabilised (BiCGStab) (Ashby and Falgout, 1996) available from the high-performance solver library HYPRE (Center for Applied Scientific Computing, 2006). A staggered numerical grid is employed for better velocity-pressure coupling. This is achieved by determining the pressure and other scalar quantities at the cell centres and the velocities are determined at the cell faces. Turbulence is modelled with the two-equation $k-\omega$ model (Wilcox, 1994) with the transport equations for the turbulent kinetic energy k and the specific turbulent dissipation rate ω are presented in Eq. (13) and (14).

$$\frac{\partial k}{\partial t} + u_j \frac{\partial k}{\partial x_j} = \frac{\partial}{\partial x_j}\left[\left(\nu + \frac{\nu_t}{\sigma_k}\right)\frac{\partial k}{\partial x_j}\right] + P_k - \beta_k k\omega \tag{13}$$

$$\frac{\partial \omega}{\partial t} + u_j \frac{\partial \omega}{\partial x_j} = \frac{\partial}{\partial x_j}\left[\left(\nu + \frac{\nu_t}{\sigma_\omega}\right)\frac{\partial \omega}{\partial x_j}\right] + \frac{\omega}{k}\alpha P_k - \beta\omega^2 \tag{14}$$

where P_k is the production rate and the closure coefficients $\sigma_k = 2$, $\sigma_\omega = 2$, $\alpha = 5/9$, $\beta = 3/40$ and $\beta_k = 9/100$ and the eddy viscosity ν_t is defined in Eq. (15).

$$\nu_t = \frac{k}{\omega} \tag{15}$$

The large strain in the flow due to wave propagation leads to unphysical overproduction of turbulence. Eddy viscosity limiters (Durbin, 2009) are used to avoid this. In a two-phase CFD model, the large difference in density at the interface between air and water causes an overproduction of turbulence at the interface. Free surface turbulence damping (Naot and Rodi, 1982) is carried out only at the interface using the Dirac delta function. REEF3D is fully parallelised using the domain decomposition strategy and MPI (Message Passing Interface). Time discretisation is performed with a third-order accurate total variation diminishing (TVD) Runge–Kutta scheme (Shu and Osher, 1988). A ghost-cell immersed boundary method based upon the local directional by Berthelsen and Faltinsen (2008) is employed to account for the solid boundaries of the fluid domain and represent complex geometries without explicitly specifying the boundary conditions. The fluid flow properties at the boundaries of the porous objects are accounted for in the same manner.

Level set method In order to obtain the free surface, the level set method (Osher and Sethian, 1988) is used. In this method, the zero level set of a signed distance function, $\phi\left(\vec{x},t\right)$ called the level set function, represents the interface between water and air. For the rest of the domain, the level set function represents the closest distance of each point in the domain from the interface and the sign distinguishes the two fluids across the interface. The level set function is defined in Eq. (16).

$$\phi(\vec{x},t)\begin{cases}>0 & if\ \vec{x}\ is\ in\ phase\ 1(Water)\\ =0 & if\ \vec{x}\ is\ at\ the\ interface\\ <0 & if\ \vec{x}\ is\ in\ phase\ 2(Air)\end{cases} \tag{16}$$

The level set function is smooth across the interface and provides a sharp description of the free surface. The values for the physical properties such as density and viscosity of the two fluids across the interface are interpolated using a Heaviside function $H(\phi)$ over a distance of $\epsilon = 2.1dx$, where dx is the grid size, around the interface as shown in Eq.(17).

$$H\left(\phi\right)=\begin{cases}0 & if\ \phi<-\epsilon\\ \frac{1}{2}\left(1+\frac{\phi}{\epsilon}+\frac{1}{\pi}sin\left(\frac{\pi\phi}{\epsilon}\right)\right) & if\ \ |\phi|<\epsilon\\ 1 & if\ \phi>\epsilon\end{cases} \tag{17}$$

This smoothens the discontinuity caused by the abrupt change in the physical properties of the fluids across the interface. The value of $\epsilon = 2.1dx$ is chosen such that at least one cell in each direction is included in the interpolation and the density profiles across the interface are smooth as shown by Bihs et al. (2016). The density at the cell face is then calculated through averaging as shown in Eq.(18).

$$\rho_{i+\frac{1}{2}}=\rho_1 H\left(\phi_{i+\frac{1}{2}}\right)+\rho_2\left(1-H\left(\phi_{i+\frac{1}{2}}\right)\right), \tag{18}$$

where ρ_1 and ρ_2 are the densities of the two phases, air and water respectively. The values of the fluid viscosity are interpolated in the same manner. To obtain the change in the free surface, the level set function is convected under the velocity field in the wave tank (Eq. 19).

$$\frac{\partial\phi}{\partial t}+u_j\frac{\partial\phi}{\partial x_j}=0 \tag{19}$$

Inside the porous media, the velocity field u_j is replaced by the filter velocity field $\frac{\langle u_j\rangle}{n}$. The signed distance property of the function is lost by the motion of the free surface and it is restored by reinitialising the function after every iteration using the partial differential equations (Peng et al., 1999).

2.3 Numerical wave tank

REEF3D can be used a numerical wave tank using the wave generation and absorption boundary conditions implemented in the model. The two major methods provided for wave generation are the relaxation method (Engsig-Karup et al., 2008) and the Dirichlet-type method. In the first method, a part of the wave tank is reserved for the purpose of wave generation

and absorption using relaxation functions. The relaxation functions then modulate the computational values with a theoretical value to either generate or absorb waves (Bihs et al., 2016). In the Dirichlet-type method, the desired values for velocities and the free surface elevation are directly prescribed at the inlet boundary. In this way, reserving additional zones in the wave tank for wave generation and absorption are avoided. The current study employs the Dirichlet-type method for wave generation and no numerical beach is used in the cases simulated in this study. A Cartesian grid is employed in the study and $dx = dy = dz$ in all the simulations.

3 Results and Discussion

Several cases are presented in this paper to validate the VRANS implementation in the numerical model with both two- and three-dimensional scenarios and investigate the wave-porous structure interaction. The following sections present the numerical results from simulating the experiments carried out by Liu et al. (1999) for dam break against a porous medium, solitary wave interaction with a porous abutment by Lara et al. (2012), regular wave interaction with a porous abutment by Lara et al. (2012) and regular wave interaction with a multi-layered breakwater section by Arntsen et al. (2003) .

3.1 Dam Break

The two-dimensional study with a dam break on a porous medium made of crushed rocks by Liu et al. (1999) is simulated. The experimental data provides the free surface evolution both inside and outside the porous medium. In the experiments, crushed rock with a median grain size $d_{50} = 0.0159$ m and porosity $n = 0.49$ is placed in the tank in the form of a porous dam with a length of 0.29 m and a height of 0.58 m. A reservoir of water is created beside the porous dam with a length of 0.28 m and the height of the reservoir is set to 0.35, 0.25 and 0.14 m in the different trials. The reservoir is separated from the porous dam with a 0.02 m thick gate which is operated manually. In addition, 0.025 m layer of water is allowed at the bottom of the tank. The numerical setup is the same as the experimental setup and is illustrated in Fig. (2). A grid size of $dx = 0.005$ m is used for this simulation.

The resistance coefficients α and β are calibrated by completing a simulation matrix, where the 2 coefficients are varied as $\alpha = [500, 650, 750, 1000, 2500]$ and $\beta = [1, 1.5, 2, 2.2, 3]$. The best agreement between the numerical and experimental results is found for the combination $\alpha = 650$ and $\beta = 2.2$. The simulated evolution of the flow through the porous dam is compared to the experimental data and presented in Fig. (3). In the initial stage of the dam break, there is a small disagreement between the experimental and numerical results especially inside the porous medium. This is due to the difference in the initial flow in the experiments and in the numerical model. In the experiments, the water is blocked with a gate and opening of the gate results in water being rushed to the porous medium. The impact of the water leads to a small upward jet on the surface of the porous medium (Liu et al., 1999). The gate is opened manually in the experiments within a finite duration (0.1s) and the water close to the bottom to moves earlier than the water at free surface. In the simulations, the dam break occurs by an instantaneous release of the water column. Thus, the entire water column is set into motion at once and explains the small difference in the calculated water surface and the observed values at $t = 0.2$ s and 0.4 s in Figs.(3b) and (3c) respectively.

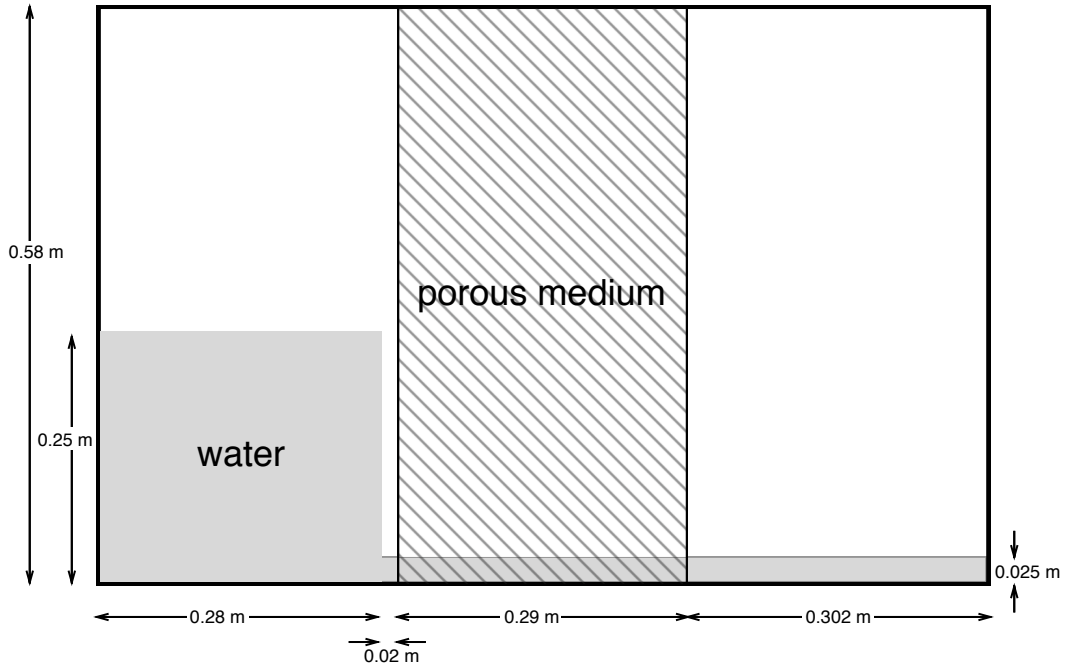

Figure 2: Dam break-setup for physical experiments

In Figs.(3d)-(3f), the flow through the porous medium is mainly due to the pressure difference and the agreement gets better as the time progresses. Figures (3g)-(3j) represent the situation where the water has reached the right wall and is reflected back. This reflected wave breaks again on the porous medium and this is captured well in the numerical model. Figure (3k)-(3l) represent the period after breaking where water on the right side oscillates a little while water from the left side is still seeping through the porous medium. The flow regime corresponds to a transition between Forchheimer and a fully turbulent flow regime and is very well represented by the model.

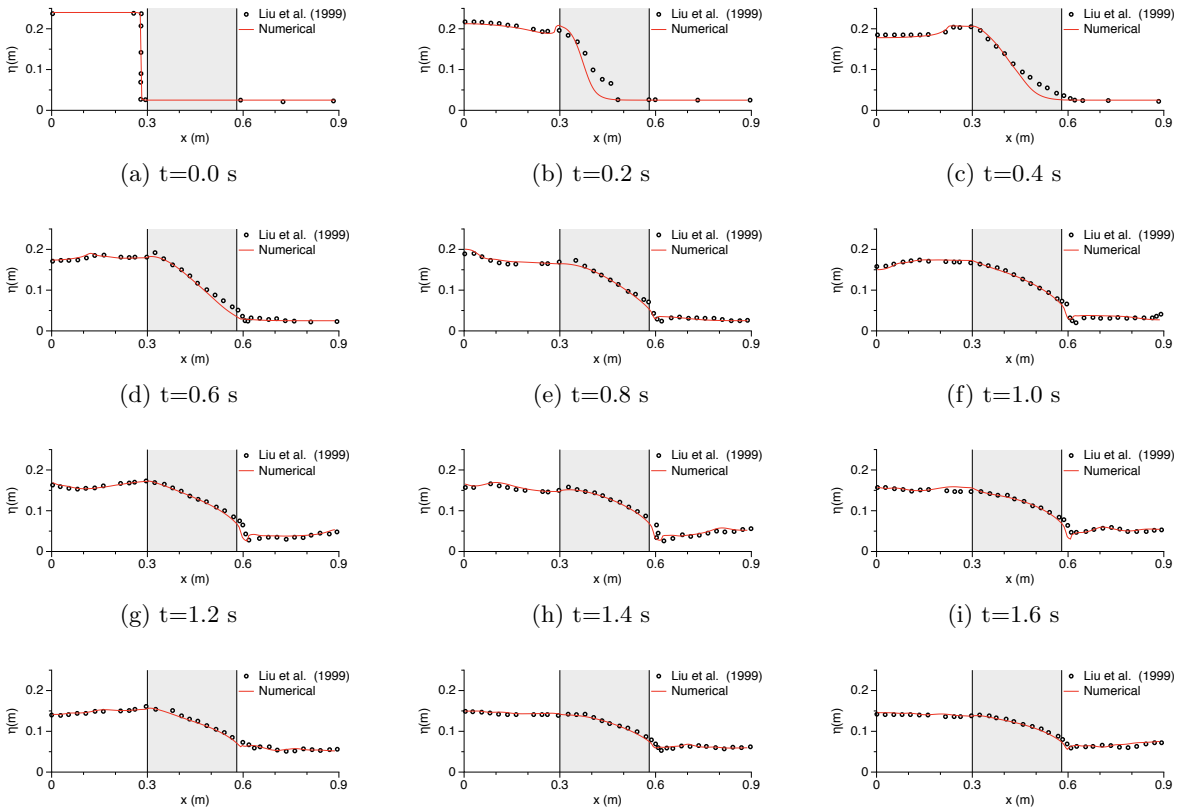

(a) t=0.0 s (b) t=0.2 s (c) t=0.4 s

(d) t=0.6 s (e) t=0.8 s (f) t=1.0 s

(g) t=1.2 s (h) t=1.4 s (i) t=1.6 s

(j) t=1.8 s (k) t=2.0 s (l) t=2.2 s

Figure 3: Free surface in the simulations and experiments for flow passing through porous dam made of crushed rock with $d_{50} = 0.0159$ m and $n = 0.49$ represented by $\alpha = 650$ and $\beta = 2.2$

3.2 Wave interaction with a porous abutment

A three-dimensional scenario with the interaction of waves with a porous abutment investigated by Lara et al. (2012) is simulated in this section. The domain is 18.2 m long, 8.6 m wide and 1.0 m high. A porous structure 4.0 m long, 0.5 m wide and 0.6 m high in a water depth $d = 0.4$ m is built using a metallic mesh filled with granular material. The median particle size of the granular material $d_{50} = 0.015$ m and porosity $n = 0.51$. The structure is placed perpendicular to the direction of wave propagation at a distance of 10.5 m from the wavemaker. The numerical setup is the same in the experiments and is illustrated in Fig. (4). As in the experiments, no beach is used in the numerical wave tank. Since the d_{50} and n values in this case are similar to the values for the dam break case in the previous section, the same values of $\alpha = 650$ and $\beta = 2.2$ are selected for the simulations in this section as well. A grid size of $dx = 0.025$ m is used in the simulation. The free surface elevation is recorded at fifteen locations in the wave basin and pressure gauges are placed at six locations on the porous structure. The exact positions of wave gauges and pressure gauges are listed in Table 2.

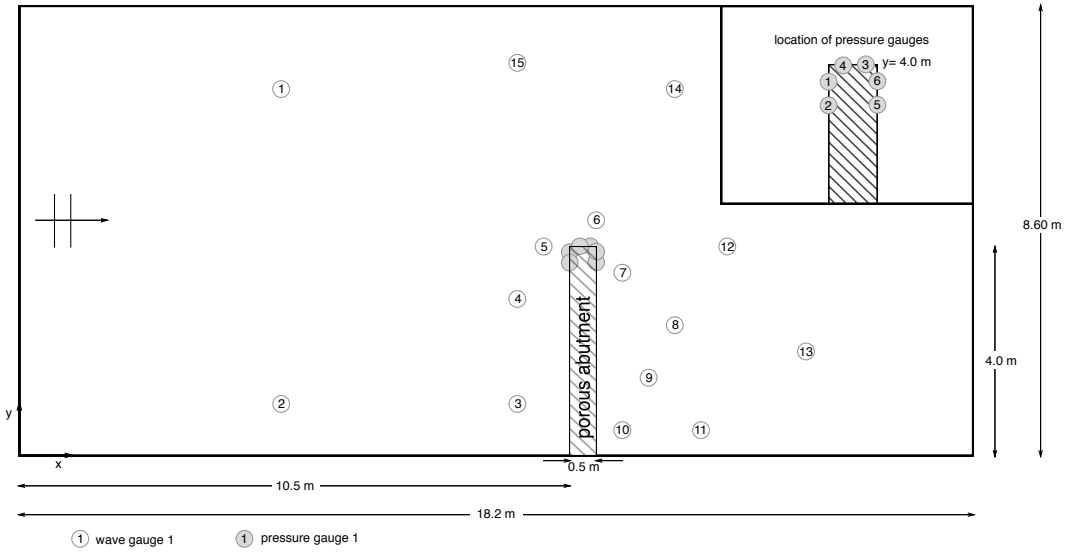

Figure 4: Numerical setup for porous abutment in wave basin, the location of the pressure gauges is shown in the inset figure

Wave Gauge	x (m)	y (m)	**Pressure Gauge**	x (m)	y (m)	z (m)
WG1	5.0	7.0	PG1	10.5	3.89	0.11
WG2	5.0	1.0	PG2	10.5	3.69	0.25
WG3	9.5	1.0	PG3	10.89	4.0	0.11
WG4	9.5	3.0	PG4	10.69	4.0	0.25
WG5	10.0	4.0	PG5	11.0	3.70	0.11
WG6	11.0	4.5	PG6	11.0	3.9	0.25
WG7	11.5	3.5				
WG8	12.5	2.5				
WG9	12.0	1.5				
WG10	11.5	0.5				
WG11	13.0	0.5				
WG12	13.5	4.0				
WG13	15.0	2.0				
WG14	12.5	7.0				
WG15	9.5	7.5				

Table 2: Location of the wave and pressure gauges in the numerical wave tank

Solitary wave interaction with a porous abutment First, the interaction of a solitary wave of height $H = 0.09$ m with the porous abutment is simulated. In the absence of a beach, the solitary wave is reflected from the end of the domain and propagates towards the wavemaker, interacting with the porous structure for a second time. The free surface elevations calculated numerically at the different locations listed in Table (2) are compared to the experimental results in Fig. (5). In Fig. (5a) the incident wave propagating towards the end of the domain and the reflected wave travelling towards the wavemaker at WG1 are

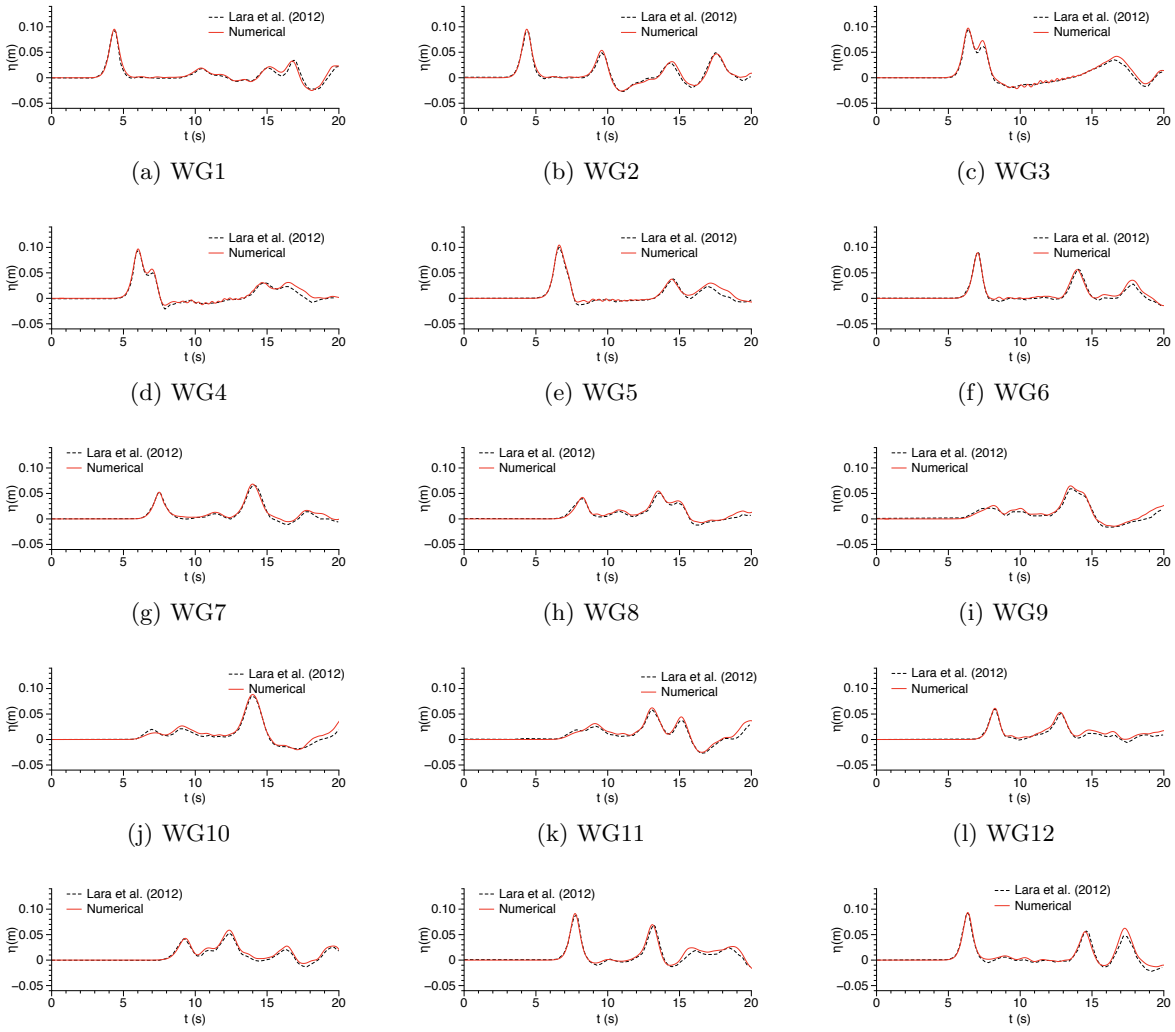

(a) WG1 (b) WG2 (c) WG3

(d) WG4 (e) WG5 (f) WG6

(g) WG7 (h) WG8 (i) WG9

(j) WG10 (k) WG11 (l) WG12

(m) WG13 (n) WG14 (o) WG15

Figure 5: Numerical and experimental results (Lara et al., 2012) for the free surface elevation for solitary wave interaction with a porous abutment

seen at at $t = 4$ s and $t = 15$ s respectively. The free surface elevation at WG2 in Fig. (5b) shows the incident wave, the partially reflected wave from the structure and the reflected wave from the end of the domain after interacting with the porous abutment. WG3 and WG4 in Figs. (5c) and (5d) respectively show a secondary crest beside the primary crest as they are placed just 1 m from the face of the porous abutment and are quickly affected by the partially reflected wave. The reflected waves from the end of the domain are partially transmitted and seen as the smaller peaks around $t = 15$ s. Wave gages WG5, WG6 and WG7 are placed around the seaward edge of the porous structure. The reduction of the incident wave height as it crosses the structure is apparent in the visual comparison of the first peaks in Fig. (5e) and (5g) corresponding to WG5 and WG7 respectively. Figures (5h)-(5k) present the free surface elevations at WG8-WG11 respectively which are on the leeward side of the

porous abutment. The wave crest calculated at these locations correspond to the incident wave that is damped by the porous structure. The second crest calculated at these locations corresponds to the reflected wave from the end of the domain. WG12 is located 2.5 m behind the seaward edge of the abutment and the incident wave consists of the unaffected part of the wave and the part transmitted through the abutment. In addition, WG12 is also fully exposed to the reflected wave from the end of the domain as seen in Fig. (5l). The free surface elevation 3 m behind the structure at WG13 in Fig. (5m) shows a damped incident wave after interaction with the structure, the reflected wave from the end of the domain followed by the partially re-reflected waves from the structure. The locations WG14 and WG15 are exposed to a mostly undisturbed incident and the reflected waves along with some radiated waves from the structure as seen in Fig. (5n) and (5o) respectively. The numerical results agree well with the experimental results both in phase and amplitude of the incident and reflected waves at the different locations.

A grid convergence study is carried out by repeating the simulation with grid sizes $dx =$ 0.03 m, $dx = 0.05$ m and 0.075 m. The numerical results for the free surface elevation at locations WG2 and WG13 are presented in Fig. (6). The two wave gauges are located on either side of the abutment and receive most of the wave action from both incident and reflected waves. It is seen that the free surface elevations for both WG2 and WG13 in Figs. (6a) and (6b) are similar for all the grid sizes used and exactly the same for $dx = 0.03$ m and $dx = 0.025$ m. Thus, the results presented using $dx = 0.025$ m are grid independent. In

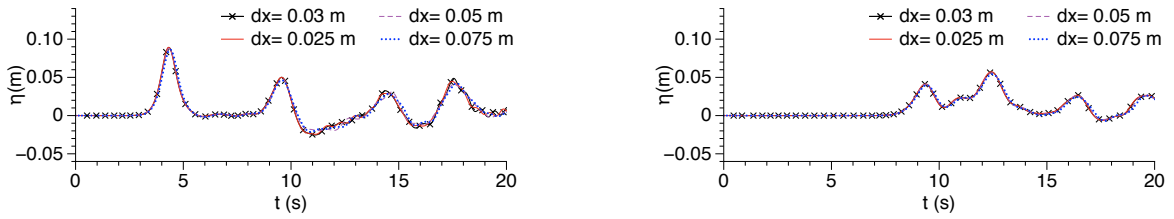

(a) free surface at WG2

(b) free surface at WG13

Figure 6: Grid convergence study for solitary wave interaction with the porous abutment

order to demonstrate the improved numerical results obtained with the current approach, a comparison with the numerical results from Lara et al. (2012) for the free surface elevation around the porous structure is presented along with the experimental data in Fig. (7). It seen that the the reflected wave at WG7 is better represented in the current model in Fig. (7a). The free surface elevations at WG10 in Fig. (7b) are similar in the current work and previously presented numerical results. At the most onshore location behind the porous abutment, WG13, the current model provides a better representation of both the amplitude and phases of the wave crests in Fig. (7c). At WG15 in Fig. (7d), the current model shows better agreement with the experimental data compared to previous numerical results. The pressure calculated at the six different locations in the porous abutment are compared to the experimental data in Fig. (8). Three distinct peaks are seen in each of the figures due to the incident wave, the transmitted wave and the reflected wave. PG1 and PG2 are placed on the seaward side and the highest peaks are seen to occur when the solitary wave is incident on the abutment in Figs. (8a) and (8b). The pressures inside the abutment measured at PG3 and PG4 are

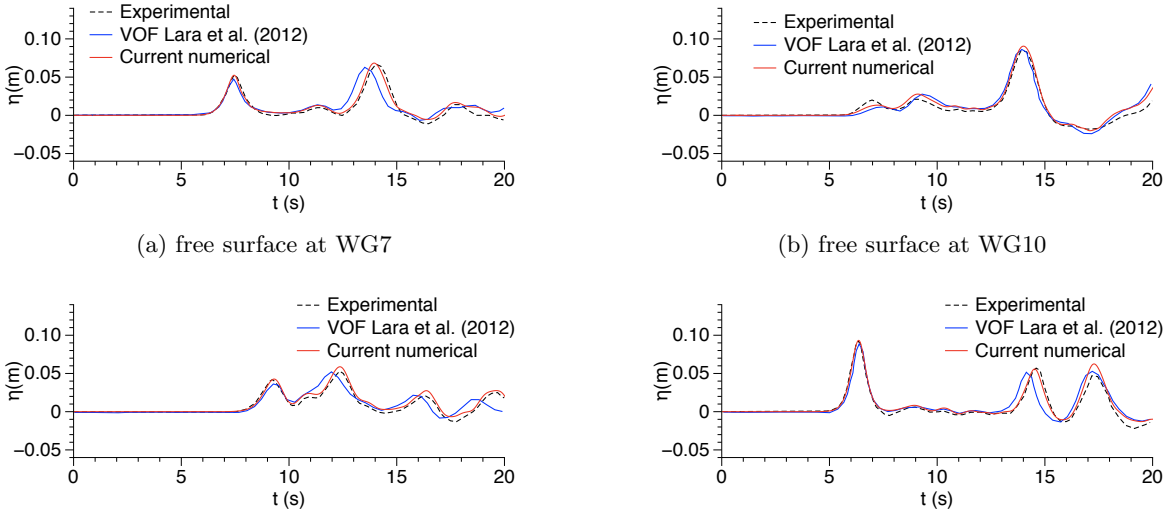

(a) free surface at WG7

(b) free surface at WG10

(c) free surface at WG13

(d) free surface at WG15

Figure 7: Comparison numerical results with the current approach with numerical results from Lara et al. (2012) and experimental data for solitary wave interaction with a porous abutment

presented in Figs. (8c) and (8d) respectively and the three peaks are seen to be of comparably similar magnitudes. On the leeward side at PG5 and PG6, the highest peaks result from the wave reflected from the end of the domain as seen in Figs. (8e) and (8f). The numerical results show a good agreement with experimental data for the measured pressures as well.

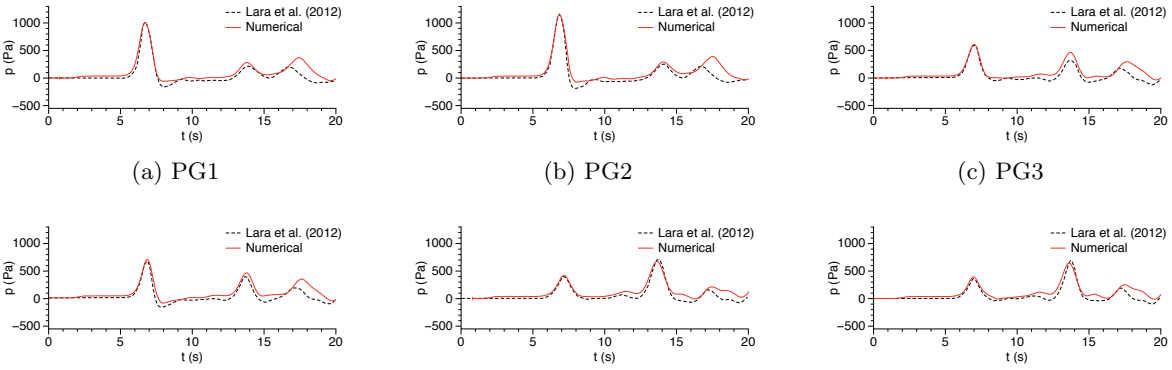

(a) PG1

(b) PG2

(c) PG3

(d) PG4

(e) PG5

(f) PG6

Figure 8: Numerical and experimental (Lara et al., 2012) pressure in the structure for solitary wave interaction with a porous abutment

The interaction of the solitary wave with the porous abutment in the numerical wave tank is presented in Fig. 9. The solitary wave approaching the porous abutment at $t = 5.0$ s is shown in Fig. (9a). At $t = 6.5$ s, the incident wavefront is separated by the abutment and the transmitted wave in the unblocked region is seen in Fig. (9b). Figure (9c) shows the

wave transmitted through and beyond the abutment approach the end of the domain and the first partially reflected wave from the abutment travelling towards the wavemaker at $t = 9.0$ s. The transmitted wave is reflected back towards the abutment at $t = 10.0$ s in Fig. (9d). The wave reflected from the end of the domain interacts with the porous abutment again at $t = 13.5$ s in Fig. (9e). Here, the wavefront is separated by the abutment for the second time resulting in transmitted waves through and beyond the abutment along with a second partially reflected wave. The first partially reflected wave is re-reflected from the wavemaker and reaches the abutment at $t = 16.5$ s, while the second partially reflected wave is near the end of the domain in Fig. (9f). The interaction processes presented in this figure can be easily identified with the different peaks observed at the different locations in Fig. (5).

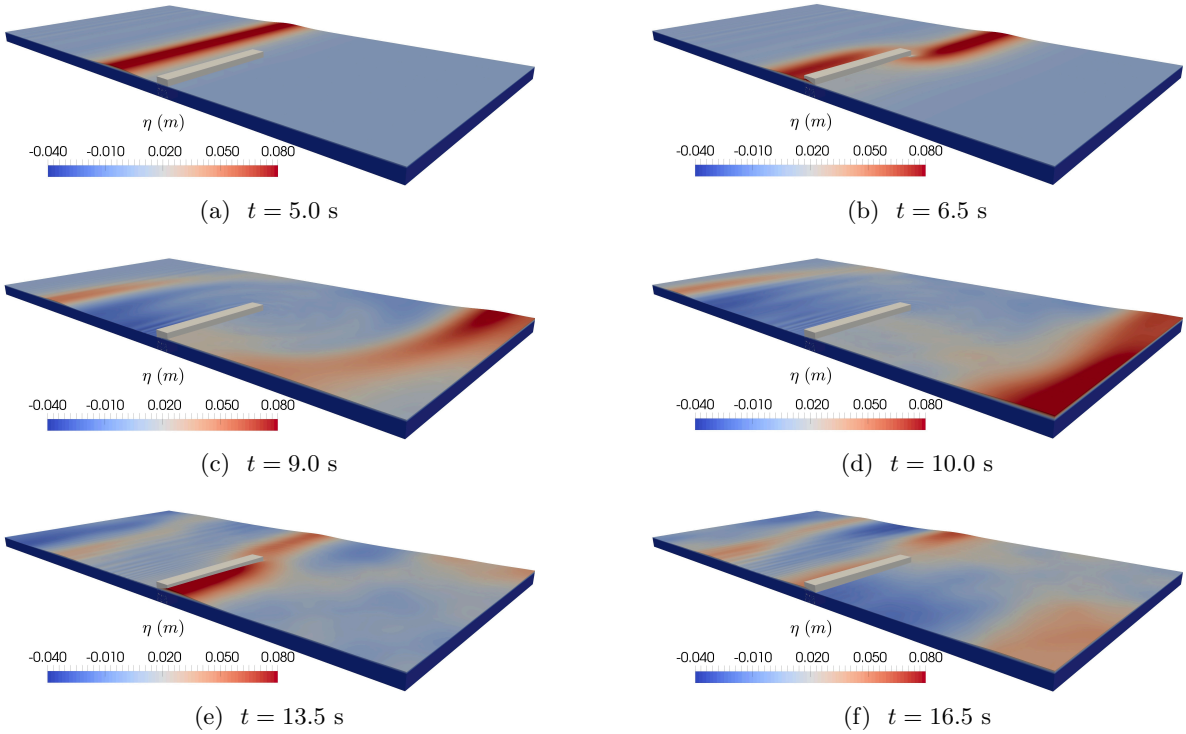

(a) $t = 5.0$ s (b) $t = 6.5$ s

(c) $t = 9.0$ s (d) $t = 10.0$ s

(e) $t = 13.5$ s (f) $t = 16.5$ s

Figure 9: Free surface elevation in the numerical wave tank for solitary wave interaction with a porous abutment

In order to demonstrate the satisfaction of the continuity at the interface between the water and the porous media, the pressure and horizontal velocity time series on either side of the weather side boundary of the porous abutment at PG8 (10.49, 3.90, 0.25) and PG9 (10.51, 3.90, 0.25) are presented in Fig. (10). It is seen that the computed pressures and velocities across the boundary are the same and the continuity condition is satisfied. In addition, the horizontal velocity profiles over the water depth far from the abutment ($x = 10.0$m), just in front of the abutment ($x = 10.49$ m), just inside the abutment ($x = 10.51$ m) and at the centre of the abutment ($x = 10.75$ m), close to the head of the abutment at $y = 3.90$ m , middle of the abutment at $y = 2.00$ m and close to the wall at $y = 0.50$ m at $t = 6.75$ s are presented in Fig. (11). The solitary wave crest is incident on the porous abutment at this instance in the simulation. The horizontal velocity profile shows the highest amplitude at the

far field location at $x = 10.0$ m in Fig. (11a), due to the fact that this location is closer to the head of the abutment and experiences the least resistance to the flow. The horizontal velocity profiles at $x = 10.0$ m are identical for $y = 2.0$ m and $y = 0.50$ m in Figs. (11b) and (11c) respectively. Also, it is seen that the maximum horizontal velocity is damped as wave travels from the far field location at $x = 10.0$ m towards the centre of the porous abutment at $x = 10.75$ m at all three locations along the length of the porous abutment.

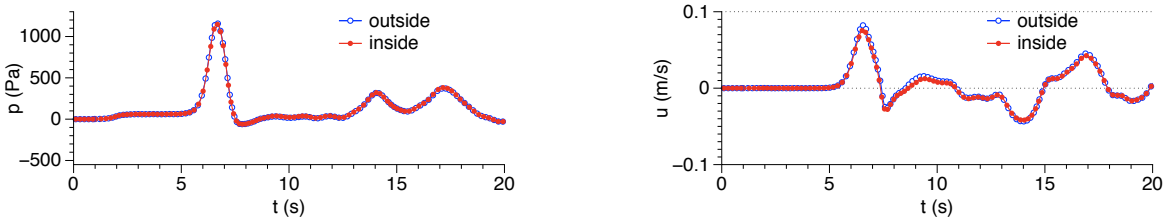

(a) computed pressure (b) computed horizontal velocity

Figure 10: Numerical results for the pressure and horizontal velocity on either side of the porous interface at PG8 and PG9 for solitary wave interaction with a porous abutment

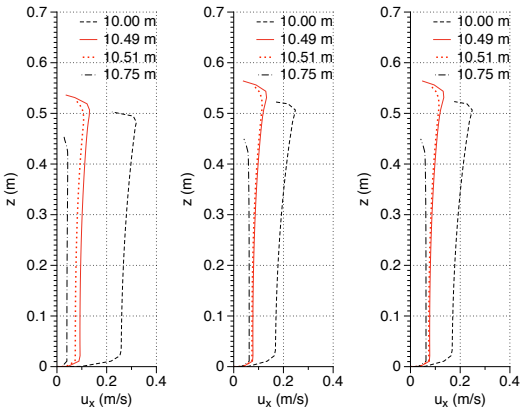

(a) $y = 3.90$ m (b) $y = 2.00$ m (c) $y = 0.50$ m

Figure 11: Horizontal velocity profiles over the water depth outside and inside the porous abutment for an incident solitary wave at various $x-$ locations for different locations along the porous abutment

Regular wave interaction with a porous abutment The interaction of the porous abutment with waves is further studied with periodic waves in the numerical wave tank. As in the experiments by Lara et al. (2012), waves of period $T = 4.0$ s and height $H = 0.09$ m are generated using cnoidal wave theory. The values for the grid size $dx = 0.025$ m and the porous media resistance coefficients $\alpha = 650$ and $\beta = 2.2$ are retained from the solitary wave simulation above. The free surface elevations calculated at the different locations listed in Table (2) are compared with the experimental results from Lara et al. (2012) in Fig. (12). The

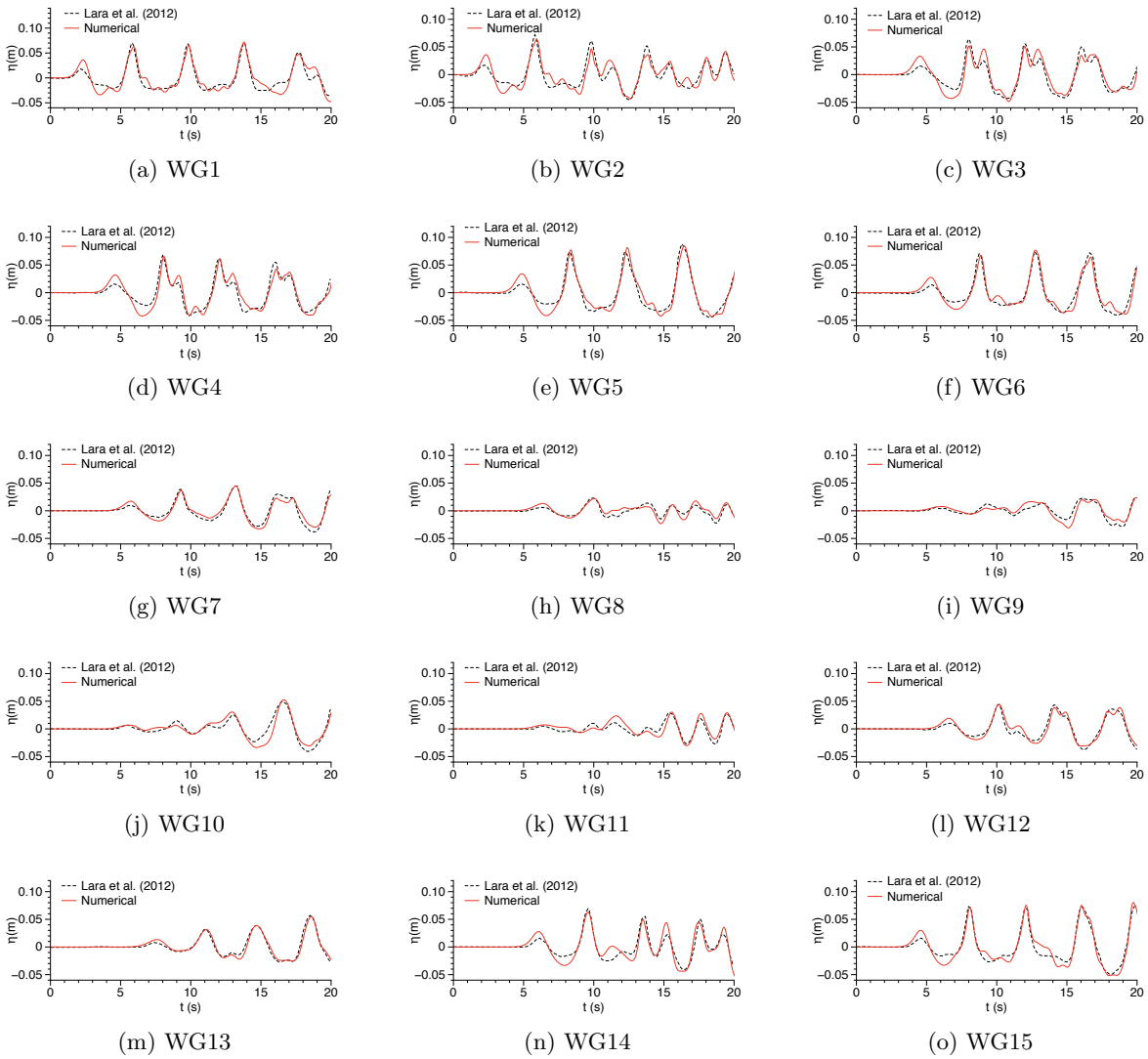

(a) WG1 (b) WG2 (c) WG3

(d) WG4 (e) WG5 (f) WG6

(g) WG7 (h) WG8 (i) WG9

(j) WG10 (k) WG11 (l) WG12

(m) WG13 (n) WG14 (o) WG15

Figure 12: Numerical and experimental results (Lara et al., 2012) for the free surface elevation regular wave ($H = 0.09$ m, $T = 4.0$ s) interaction with a porous abutment

present scenario with regular waves involves more interactions compared to the solitary wave scenario due to the periodic nature of the incident waves. First, the wave is partially reflected and transmitted through and beyond the abutment. The transmitted wave is reflected from the end of the domain and interacts with the following wave. This transformed wave then interacts with the abutment again, resulting in further transmission towards the wavemaker and partial reflection towards the end of the domain. This process repeats itself over the course of the simulation resulting in complex wave patterns. At locations close to the abutment on the upstream side, several peaks in the wave crests are observed like in Figs. (12b), (12c) and (12d). At locations on the leeside of the abutment, cancellation of the transmitted and reflected waves result in periods of near-zero elevations as seen in Figs. (12h), (12i), (12j) and (12k). The complex wave-wave and wave-structure interactions are well accounted for in the

model and the numerical results are seen to be in good agreement with the experimental data at all locations.

A grid convergence study is carried out by repeating the simulation with grid sizes $dx =$ 0.03 m, $dx = 0.05$ m and 0.075 m. The numerical results for the free surface elevation at locations WG2 and WG13 are presented in Fig. (13). The two wave gauges are located on either side of the abutment and placed such that they receive most of the wave action from both incident and reflected waves. It is seen that the free surface elevations for both WG2 and WG13 in Figs. (13a) and (13b) are similar for all the grid sizes used and exactly the same for $dx = 0.03$ m and $dx = 0.025$ m. Thus, the results presented using $dx = 0.025$ m are grid independent. The numerical results for the free surface elevation at selected locations around

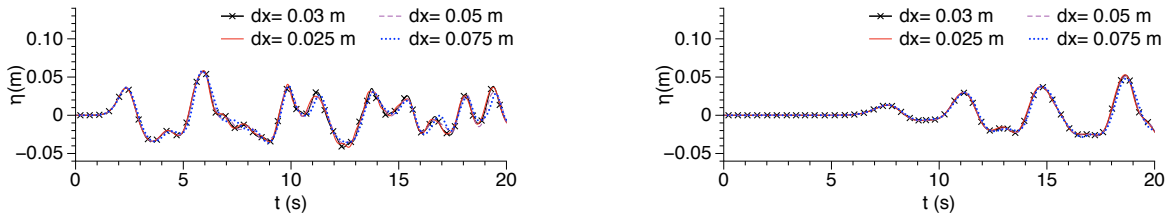

(a) free surface at WG2

(b) free surface at WG13

Figure 13: Grid convergence study for periodic wave interaction with the porous abutment

the porous abutment using the current model are compared with the numerical results from Lara et al. (2012) along with the experimental results in Fig. (14). The free surface elevations at WG7 in Fig. (14a) show that the current approach agrees better with the experimental data whereas spurious wave crests are seen in the previous numerical results. At WG10 in Fig. (14b), the current model represents every wave crest right behind the porous abutment, where both transmitted wave through the porous abutment and the reflected wave from the end of the domain are seen. A change in phase and amplitude, with spurious crests is seen at WG13 in the previous numerical results, whereas the current model follows the experimental observations in Fig. (14c). At WG15 in Fig. (14d), the current results show good agreement with the experimental data whereas previous results show an increase in the wave crest elevation over time. The pressures calculated at the six different locations in the porous abutment listed in Table (2) are compared with the experimental results in Fig. (15). The largest pressures are measured on the upstream side of the abutment at PG1 and PG2 shown in Fig. (15a) and (15b). The pressures are slightly reduced inside the abutment as seen in Fig. (15c) and (15d). On the leeside of the abutment, the pressures are initially small and increase when the reflected waves from the end of the domain are incident on the abutment in Fig. (15e) and (15f). The numerical results are seen to agree well with the experimental data in both phase and amplitude, showing that the model represents the physics involved in the flow through porous media well.

The periodic wave interaction with the porous abutment in the numerical wave tank is presented in Fig. 16, following the propagation of the second wave crest along the wave tank. The incidence of the second wave crest on the porous abutment at $t = 9.5$ s with the partially reflected wave and the transmitted wave is shown in Fig. (16a). At $t = 10.0$ s, the partially reflected wave is travelling towards the wavemaker and the transmitted wave is propagating

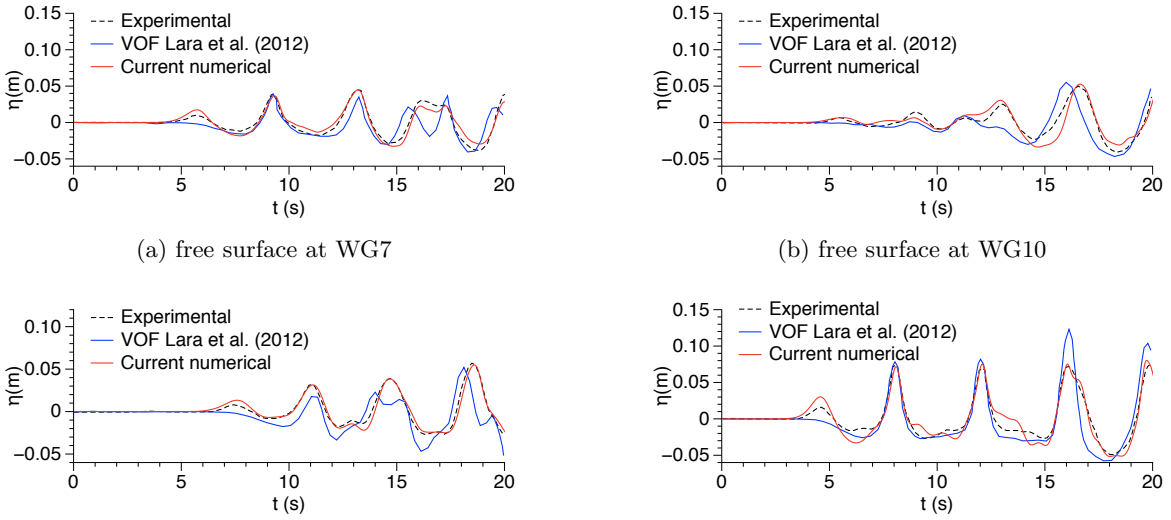

(a) free surface at WG7

(b) free surface at WG10

(c) free surface at WG13

(d) free surface at WG15

Figure 14: Comparison of numerical results with the current approach with numerical results from Lara et al. (2012) and experimental data for solitary wave interaction with a porous abutment

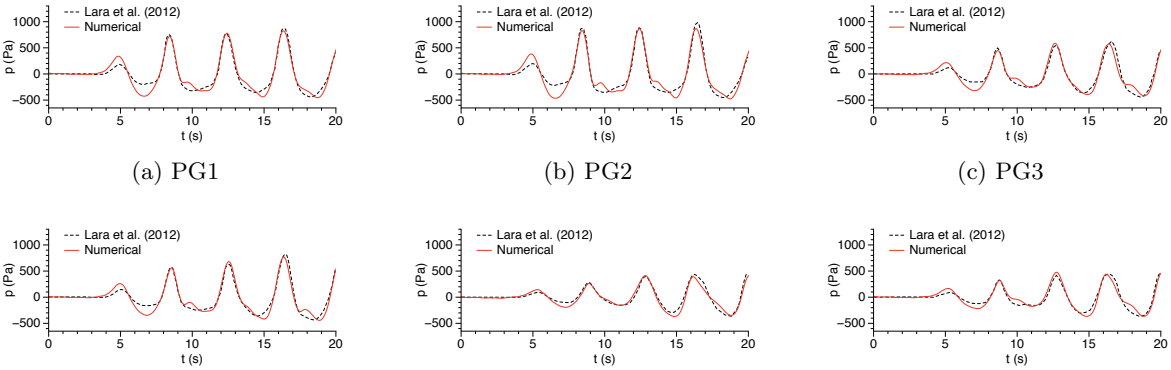

(a) PG1

(b) PG2

(c) PG3

(d) PG4

(e) PG5

(f) PG6

Figure 15: Numerical and experimental (Lara et al., 2012) pressure in the structure for regular wave interaction with a porous abutment

towards the end of the domain in Fig. (16b). Figure (16c) shows the interaction of the partially reflected wave with the next wave crest upstream of the abutment at $t = 11.0$ s. The transmitted wave interacts with the crest of the first wave crest reflected from the end of the domain downstream of the abutment in Fig. (16d)at $t = 11.5$ s. The third wave crest is incident on the abutment at $t = 12.5$ s in Fig. (16e). Here the part of the wavefront towards the landfast side of the abutment is slightly damped due to its interaction with the partially reflected wave. The first wave crest reflected from the end of the domain is incident on the lee side of the abutment while the second crest is at the end of the domain. Figure (16f) shows the incidence of the third wave crest on the abutment, while the second wave crest travels

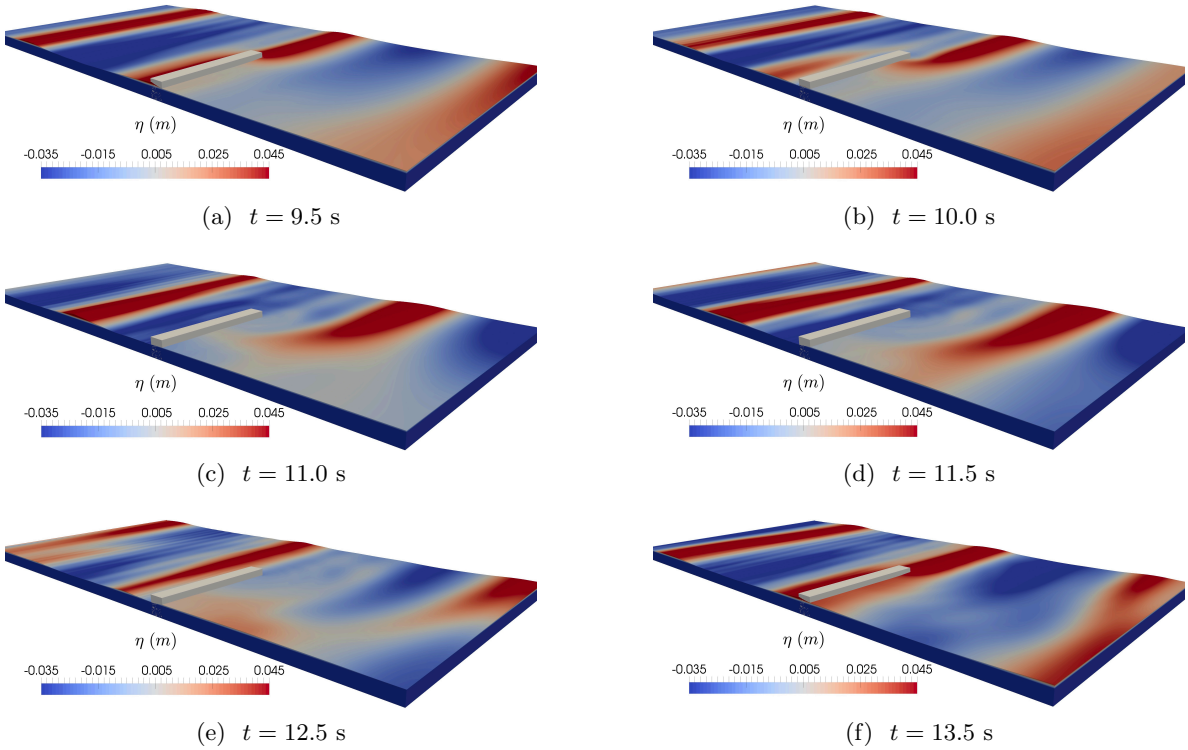

(a) $t = 9.5$ s (b) $t = 10.0$ s

(c) $t = 11.0$ s (d) $t = 11.5$ s

(e) $t = 12.5$ s (f) $t = 13.5$ s

Figure 16: Free surface elevation in the numerical wave tank for periodic wave ($H = 0.09$ m, $T = 4.0$ s) interaction with a porous abutment

towards the abutment after reflecting from the end of the domain at $t = 13.5$ s. The interaction processes presented in this figure show the additional complexities in the hydrodynamics due to the periodic waves in comparison to the solitary waves and the processes visualised in this figure can be correlated to the wave elevations at the different locations discussed in Fig. (12).

3.3 Wave interaction with a rubble mound breakwater

In this section, a rubble mound breakwater is simulated considering the porous media flow through the armour, filter and core layers in a two-dimensional numerical wave tank. The numerical results for the pore pressure are compared to the data from the experiments conducted at the SINTEF/NTNU Trondheim hydraulic laboratory by Arntsen et al. (2003). The rubble mound breakwater model has a front slope of $1 : 1.25$, 3 m long and a crest height of 1.1 m. The core is made of well-graded sand with $d_{50} = 0.0028$ m and porosity $n = 0.414$. The filter layer is 0.10 m thick and made of gravel with $d_{n50} = 0.02$ m and porosity $n = 0.33$. The armour layer is composed of one layer of stones with median weight W_{50} of about 1 kg. The median particle size is $d_{n50} = 0.07$ m and the porosity is $n = 0.30$. Inside the breakwater, pressure cells are installed to measure the pore pressure variations. The rubble mound breakwater model is illustrated in Fig. (17) along with the position of the pressure cells inside the breakwater. The locations of the pressure cells used in the experiments are listed in Table (3). Pore pressure cells P1 and P5 are placed at the boundary between the armour and the filter layers. P2 and P6 are placed at the boundary between the filter and the core layers.

P3, P4, P7 and P8 are placed in the core. The pressure cells P1, P2, P3, P4 are placed along $z = 0.25$ m above the bottom of the wave tank, and the pressure cells P5, P6, P7 and P8 are placed at a higher elevation of $z = 0.45$ m above the bottom of the tank. This provides further insight into the wave-porous structure interaction problem. Also, these measurements provide crucial data to validate the model for porous media flow through complex geometry.

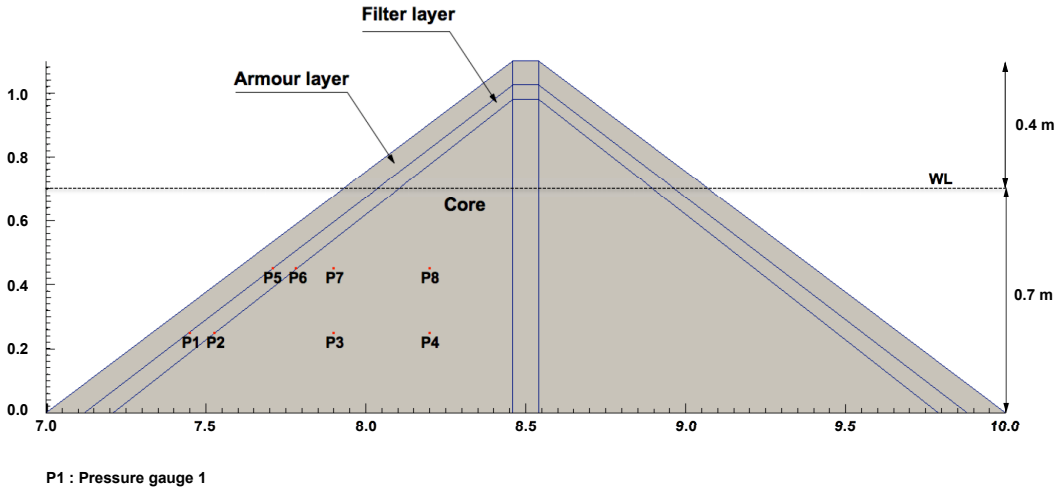

Figure 17: Illustration of the rubble mound breakwater model with three layers and the location of the pressure probes

Table 3: Position of pressure cells inside the rubble mound breakwater

Cell	PG1	PG2	PG3	PG4	PG5	PG6	PG7	PG8
x (m)	7.45	7.525	7.90	8.20	7.70	7.78	7.90	8.20
z (m)	0.25	0.25	0.25	0.25	0.45	0.45	0.45	0.45

The simulations are carried out in a numerical wave tank that is 12 m long and 1.4 m high with a grid size of $dx = 0.005$ m. The toe of the breakwater is placed $x = 7$ m away from the wave generation boundary (Fig.18). The resistance coefficients α and β are defined based on the calibrated values from the previous sections and from literature (Troch, 2000). The material characteristics and the resistance coefficients of the different layers of the breakwater are presented in Table 4. Regular waves with $H = 0.22$ m, $T = 1.5$ s are generated using the $5th$-order Stokes theory in a water depth $d = 0.7$ m.

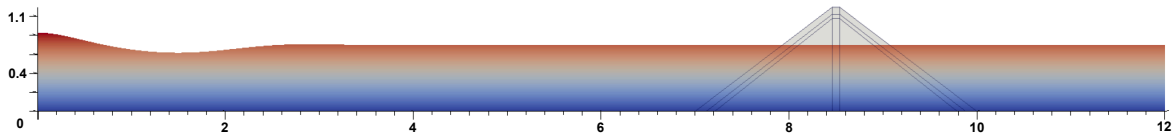

Figure 18: Setup for Rubble mound breakwater in the NWT

Table 4: Resistance coefficients for different layers in the breakwater

Layer	$d_{50}(m)$	n (-)	α (-)	β (-)
Armour	0.0596	0.3	100	1.1
Filter	0.02	0.33	600	1.1
Core	0.0028	0.414	50	2

The pore pressures calculated in the simulations at the locations listed in Table (3) are compared with the pore pressures measured at these locations in the experiments in Fig. (19). The peak pore pressures at $z = 0.25$ m above the bottom of the tank are as follows. At location P1, the boundary between the armour and filter layers, the peak pore pressure is calculated to be 525 Pa, while a pressure of 460 Pa is measured in the experiments with an overestimation of 14% as shown in Fig. (19a). At location P2, the boundary between the filter and core layers at $z = 0.45$ m in Fig. (19b), the numerical and measured values for the peak pore pressure are seen to be 470 Pa and 500 Pa respectively. The numerical model overestimates the peak pore pressure by about 6%. The deviations at these locations can be attricbuted to the averaged bulk representation of the porous resistance in the model compared to the instantaneous measurements. In addition, the locations are the boundary between two different porous layers and the numerical values for pressure are further averaged depending on the porous resistance in each of the neighbouring cells. Inside the core layer, at locations P3 and P4 in Figs. (19c) and (19d), the difference in the numerical results and the measurements is about 7% and 3% respectively. The following observations are made for the peak pore pressures at the locations closer to the free surface at $z = 0.45$ m. The numerically calculated peak pore pressure at location P5 at the boundary between the armour and filter layers is 530 Pa, and is within 1% of the measured values as seen in Fig. (19e). At the boundary between the filter and core layers at location P6 in Fig. (19f), the numerical peak pore pressure is 520 Pa and within 2% of the measured values. In the core layer at locations P7 and P8 in Figs. (19g) and (19h), values for the numerical peak pore pressure are 470 Pa and 420 Pa respectively. The numerical values are within 1% of the measurements. Overall, the numerical model calculates the pore pressures at the different locations with good accuracy. The maximum deviation between the measurements and the numerical calculations are of the order of the pressure exerted by water in one grid cell, that is 0.005 m.

The wave interaction with the porous rubble mound breakwater over half a wave period is presented in Fig. (20). The wave crest approaching the breakwater is shown in Fig. (20a). The wave crest impacts the armour layer in Fig. (20b) and the truncation of the wave crest due to the dissipation of a part of the incident wave energy is seen. The wave run up on the breakwater and the seepage into the breakwater is seen in Fig. (20c) and the process of wave run down begins in Fig. (20d). The effect of the porosity imposed by the VRANS formulation to represent the flow through three different porous layers of the breakwater is clearly seen from the velocity contours in Fig. (20). The reduction of the velocity contours and the lower values of the pore pressures measured in the core layer demonstrate that most of the wave energy is dissipated within the armour and filter layers of the breakwater and a small amount of flow seeps into the core layer.

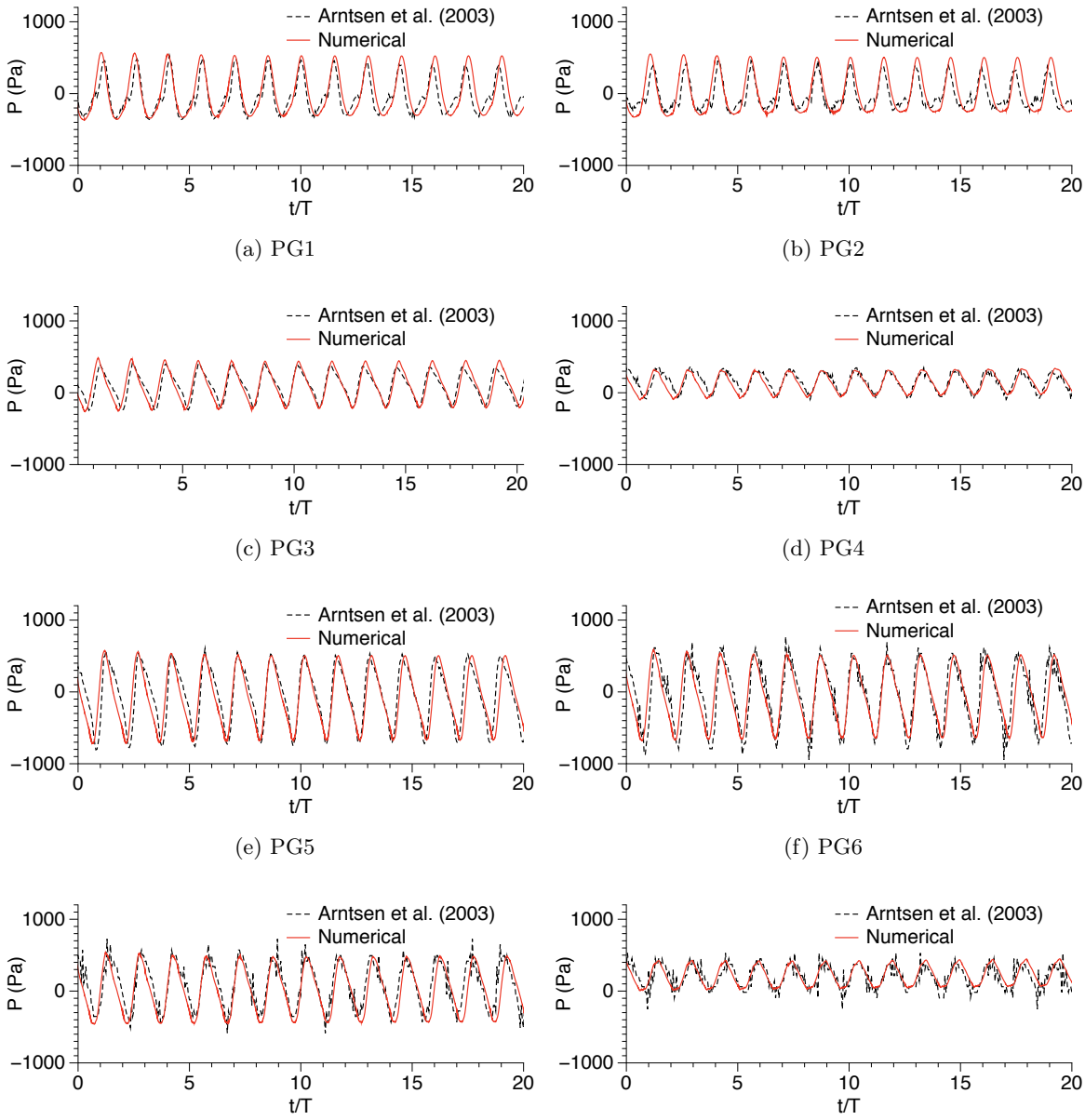

(a) PG1 (b) PG2

(c) PG3 (d) PG4

(e) PG5 (f) PG6

(g) PG7 (h) PG8

Figure 19: Comparison of pressure measurements for pressure gauges inside rubble mound breakwater for regular waves. Red lines indicate numerical model results and black lines represent experimental results

4 Conclusion

The open-source CFD model REEF3D is validated for the wave-porous structure interactions with the newly implemented VRANS method. A brief overview of the derivation of the VRANS equations is presented based on the formulations derived by Jensen et al. (2014). The

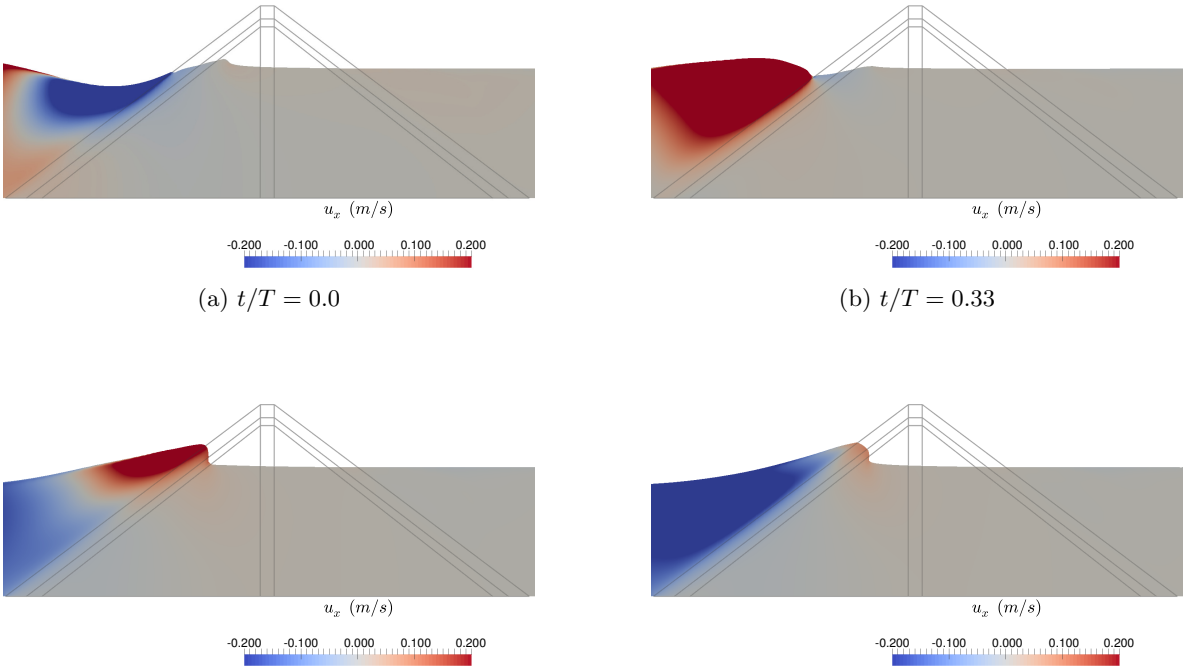

(a) $t/T = 0.0$ (b) $t/T = 0.33$

(c) $t/T = 0.50$ (d) $t/T = 0.67$

Figure 20: Wave interaction with a rubble mound breakwater simulated with three porous layers

model uses higher-order schemes for convection and temporal discretisation on a Cartesian grid along with the level set method for the free surface.

The numerical model is validated with two- and three-dimensional simulations for different flow conditions. The flow through a porous medium made of crushed rock is calculated and the free surface evolution is compared to the experimental data from Liu et al. (1999) in a 2D simulation. The numerical results agree with the experimental observations after the first 0.4 s due to the small difference in the dam break mechanism. The interaction of solitary and regular waves with a uniform porous abutment is studied in three-dimensional simulations. The numerical results for the free surface at various locations in the wave tank and the pore pressures at different locations in the porous abutment are compared with experimental data from Lara et al. (2012) and a good agreement is seen for both cases. As the properties of the porous medium are the same for the dam break scenario and the porous abutment, the same resistance coefficients are used in the three simulations. The numerical results consistently match the experimental observations, demonstrating the reliability of the numerical model in the prediction of flow through porous media. The current results show a significantly better agreement to the experimental data for solitary and regular wave interaction with a porous abutment compared to numerical results in current literature.

The numerical model is then used to simulate wave interaction with a rubble mound breakwater with three layers with different material properties. The measured pore pressures in the different layers by Arntsen et al. (2003) are compared to the numerical results. The

difference between the numerically calculated pore pressures and the measured values at all the locations closer to the crest of the breakwater is within 1%. A difference of 14% is seen at the boundary between the armour and filter layers at the location closer to the bed. This corresponds to the pressure due to a water height of 0.005 m. At other locations closer to the bed, the pressure values are within 7%of the measurements. The dissipation of the incident wave energy by the rubble mound breakwater with three porous layers is well represented by the numerical model. Overall, the numerical model demonstrates that it can reliably predict the flow through porous media and represent the fluid-structure interaction in a physical manner.

Acknowledgements

This research utilised computational facilities provided at NTNU by the Norwegian Metacenter for Computing (NOTUR) under project no. NN2620K.

References

Arntsen, Ø.A., Malmedal, I.J., Brørs, B. and Tørum, A. (2003). Numerical and experimental modelling of pore pressure variation within a rubble mound breakwater. In: *Proceedings of the International Conference on Port and Ocean Engineering Under Arctic Conditions*.

Ashby, S.F. and Falgout, R.D. (1996). A parallel mulitgrid preconditioned conjugate gradient algorithm for groundwater flow simulations. *Nuclear Science and Engineering*, **124**(1), 145–159.

Berthelsen, P.A. and Faltinsen, O.M. (2008). A local directional ghost cell approach for incompressible viscous flow problems with irregular boundaries. *Journal of Computational Physics*, **227**, 4354–4397.

Bihs, H., Alagan Chella, M., Kamath, A. and Arntsen, Ø.A. (2017). Numerical investigation of focused waves and their interaction with a vertical cylinder using REEF3D. *Journal of Offshore Mechanics and Arctic Engineering*, **139**(4), 041101–1–8.

Bihs, H. and Kamath, A. (2017). A combined level set/ghost cell immersed boundary representation for floating body simulations. *International Journal for Numerical Methods in Fluids*, **83**(12), 905–916.

Bihs, H., Kamath, A., Alagan Chella, M., Aggarwal, A. and Arntsen, Ø.A. (2016). A new level set numerical wave tank with improved density interpolation for complex wave hydrodynamics. *Computers & Fluids*, **140**, 191–208.

Burcharth, H.F. and Christensen, C. (1995). On stationary and non-stationary porous flow in coarse granular materials. *MAST G6-S, Aalborg University*, **89**(3), 327–333.

Center for Applied Scientific Computing (2006). *HYPRE high performance preconditioners - User's Manual*. Lawrence Livermore National Laboratory.

Chorin, A. (1968). Numerical solution of the Navier-Stokes equations. *Mathematics of Computation*, **22**, 745–762.

Darcy, H. (1856). *Les fontaines publiques de la ville de Dijon: exposition et application des principes à suivre et des formules à employer dans les questions de distribution d'eau, etc.* Victor Dalmont.

del Jesus, M., Lara, J.L. and Losada, I.J. (2012). Three-dimensional interaction of waves and porous coastal structures: Part i: Numerical model formulation. *Coastal Engineering*, **64**, 57–72.

Durbin, P.A. (2009). Limiters and wall treatments in applied turbulence modeling. *Fluid Dynamics Research*, **41**, 1–18.

Dybbs, A. and Edwards, R.V. (1984). Fundamentals of transport phenomena in porous media. *Journal of Computational Physics*, **41**(183), 199–256.

Engelund, F. (1953). On the laminar and turbulent flow of ground water through homogeneous sand. *Transactions of the Danish Academy of Technical Sciences 3l.*, **7**(5), 293–306.

Engsig-Karup, A.P., Hesthaven, J.S., Bingham, H.B. and Warburton, T. (2008). Dg-fem solution for nonlinear wave-structure interaction using boussinesq-type equations. *Coastal Engineering*, **55**(3), 197–208.

Forchheimer, P.H. (1901). Wasserbewegung durch boden. *Zeitz. Ver. Duetch Ing.*, **45**, 1782 –1788.

Fuhrman, D.R., Bingham, H.B. and Madsen, P.A. (2005). Nonlinear wave–structure interactions with a high-order boussinesq model. *Coastal engineering*, **52**(8), 655–672.

Garcia, N., Lara, J. and Losada, I. (2004). 2-d numerical analysis of near-field flow at low-crested permeable breakwaters. *Coastal Engineering*, 991–1020.

Gray, W. (1975). A derivation of the equations for multi-phase transport. *Chemical Engineering Science*, **30**, 229–233.

Gui, Q., Dong, P., Shao, S. and Chen, Y. (2015). Incompressible sph simulation of wave interaction with porous structure. *Ocean Engineering*, **110**, 126–139.

Higuera, P., Lara, J.L. and Losada, I.J. (2014). Three-dimensional interaction of waves and porous coastal structures using OpenFOAM®. Part i: Formulation and validation. *Coastal Engineering*, **83**, 243–258.

Higuera, P., Lara, L.J. and Losada, I.J. (2013). Simulating coastal engineering processes with OpenFOAM. *Coastal Engineering*, **71**, 119–134.

Hsu, T.J., Sakakiyama, T. and Liu, P.L.F. (2002). A numerical model for wave motions and turbulence flows in front of a composite breakwaterr. *Coastal Engineering*, **46**, 25–50.

Hu, K., Mingham, C.G. and Causon, D.M. (2000). Numerical simulation of wave overtopping of coastal structures using the non-linear shallow water equations. *Coastal engineering*, **41**(4), 433–465.

Jacobsen, N.G., van Gent, M.R.A. and Wolters, G. (2015). Numerical analysis of the interaction of irregular waves with two dimensional permeable coastal structures. *Coastal Engineering*, **102**, 13–29.

Jensen, B., Jacobsen, N.G. and Christensen, E.D. (2014). Investigations on the porous media equations and resistance coefficients for coastal structures. *Coastal Engineering*, **84**, 56–72.

Jiang, G.S. and Shu, C.W. (1996). Efficient implementation of weighted ENO schemes. *Journal of Computational Physics*, **126**, 202–228.

Kamath, A., Alagan Chella, M., Bihs, H. and Arntsen, Ø.A. (2017*a*). Energy transfer due to shoaling and decomposition of breaking and non-breaking waves over a submerged bar. *Engineering Applications of Computational Fluid Mechanics*, **11**(1), 450–466.

Kamath, A., Bihs, H. and Arntsen, Ø.A. (2017*b*). Study of water impact and entry of a free falling wedge using computational fluid dynamics simulations. *Journal of Offshore Mechanics and Arctic Engineering*, **139**(3), 031802.

Kobayashi, N. and Wurjanto, A. (1989). Wave transmission over submerged breakwaters. *Journal of waterway, port, coastal, and ocean engineering*, **115**(5), 662–680.

Lara, J.L., del Jesus, M. and Losada, I.J. (2012). Three-dimensional interaction of waves and porous structures part ii: Experimental validation. *Coastal Engineering*, **75**, 24–46.

Lara, J.L., Garcia, N. and Losada, I.J. (2006). Rans modelling applied to random wave interaction with submerged permeable structures. *Coastal Engineering*, **53**, 395–417.

Li, T., Troch, P. and de Rouck, J. (2004). Wave overtopping over a sea dike. *Journal of Computational Physics*, **198**(2), 686–726.

Liu, P.L.F., Lin, P., Chang, K.A. and Sakakiyama, T. (1999). Numerical modeling of wave interaction with porous structures. *Journal of waterway, port, coastal, and ocean engineering*, **125**(6), 322–330.

Liu, Z.B., Fang, K.Z. and Cheng, Y.Z. (2018). A new multi-layer irrotational boussinesq-type model for highly nonlinear and dispersive surface waves over a mildly sloping seabed. *Journal of Fluid Mechanics*, **842**, 323–353.

Madsen, P.A., Murray, R. and Sørensen, O.R. (1991). A new form of the boussinesq equations with improved linear dispersion characteristics. *Coastal Engineering*, **15**, 371–388.

Naot, D. and Rodi, W. (1982). Calculation of secondary currents in channel flow. *Journal of the Hydraulic Division, ASCE*, **108**(8), 948–968.

Ong, M.C., Kamath, A., Bihs, H. and Afzal, M.S. (2017). Numerical simulation of free-surface waves past two semi-submerged horizontal circular cylinders in tandem. *Marine Structures*, **52**, 1–14.

Osher, S. and Sethian, J.A. (1988). Fronts propagating with curvature- dependent speed: algorithms based on Hamilton-Jacobi formulations. *Journal of Computational Physics*, **79**, 12–49.

Peng, D., Merriman, B., Osher, S., Zhao, H. and Kang, M. (1999). A PDE-based fast local level set method. *Journal of Computational Physics*, **155**, 410–438.

Polubarinova-Kochina, P.Y. (1962). Theory of ground water movement. *Princeton University Press, Princeton, N.J.*, **10**, 252–271.

Ren, B., Wen, H., Dong, P. and Wang, Y. (2016). Improved sph simulation of wave motions and turbulent flows through porous media. *Coastal Engineering*, **107**, 14–27.

Shao, S. (2010). Incompressible sph flow model for wave interactions with porous media. *Coastal Engineering*, **57**(3), 304–316.

Shu, C.W. and Osher, S. (1988). Efficient implementation of essentially non-oscillatory shock capturing schemes. *Journal of Computational Physics*, **77**, 439–471.

Troch, P. (2000). *Experimentele studie en numerieke modellering van golfinteractie met stort-steengolfbrekers*. Ph.D. thesis, Ghent University, Belgium.

van Gent, M.R.A. (1993). *Stationary and oscillatory flow through coarse porous media*. TU Delft.

van Gent, M.R.A. (1995). *Wave interaction with permeable coastal structures*. Ph.D. thesis, Delft University of Technology, The Netherlands.

Wilcox, D.C. (1994). *Turbulence modeling for CFD*. DCW Industries Inc., La Canada, California.